Novel Asymmetric T-Shaped Radiating Element for Circularly-Polarized Waveguide Slot Arrays

Jose I. Herranz-Herruzo, *Member, IEEE*, Miguel Ferrando-Rocher, *Member, IEEE*, Alejandro Valero-Nogueira, *Senior Member, IEEE*, and Bernardo Bernardo-Clemente

***Abstract*—Waveguide slot arrays are a widely used solution to attain linearly-polarized high-gain antennas. In this paper, an all-metal T-shaped radiating element is conceived with the aim to replace the usual rectangular slots and attain circularly-polarized arrays, preserving their good properties. The polarization conversion is made possible thanks to the inclusion of a parasitic arm perpendicular to the main active slot. Due to the fact that this second arm is not directly fed by the waveguide but coupled to the active slot, the T-shaped element can be used in any array originally formed by metallic rectangular slots. The design of resonant shunt arrays has been addressed here for validation purposes. The experimental results of two sample linear arrays at 30 GHz demonstrate the design accuracy and manufacturing reliability, reporting an axial ratio below 2 dB within a bandwidth of 1.9 GHz and a peak efficiency around 98%.**

***Index Terms*—Antenna arrays, circular polarization, slotted waveguide arrays.**

I. Introduction

SLOT arrays fed by hollow waveguides have become a widespread and convenient antenna solution for a large variety of applications at the millimeter-wave band, such as radar, remote sensing or high-data-rate communications. This kind of antennas stand out for their planar profile, geometric simplicity, structural robustness, high efficiency and power handling, narrow beamwidth, good crosspolar discrimination and low sidelobe level.

However, the conversion of a classic all-metal linearly-polarized (LP) slot array into a circularly-polarized (CP) antenna, increasingly demanded by modern mm-wave systems, is not trivial at all. One of the most successful approaches consists of using dual-mode shaped apertures as radiating elements. In these cases, intricate multilayer corporate-feed networks are usually adopted to properly feed the radiators via coupling cavities, leading to a wideband radiation performance [1]–[3]. More classic and simpler solutions [4], [5] arrange crossed or shaped slots operating in a leaky-wave mode to avoid grating lobes.

Printed technologies offer an appealing alternative to hollow waveguides due to their lower profile, weight and cost, and their versatility to conceive wideband CP radiators. A large variety of array samples can be found in literature, either multilayer corporate-fed arrays [6]–[9] or simpler beam-squint traveling and leaky-wave arrays [10]–[14]. Despite its demonstrated good performance in terms of axial ratio (AR) bandwidth, arrays fed by dielectric-filled waveguides suffer from moderate dielectric losses in high frequencies, and provide lower power handling capability and mechanical robustness, when compared to those fed by hollow waveguides.

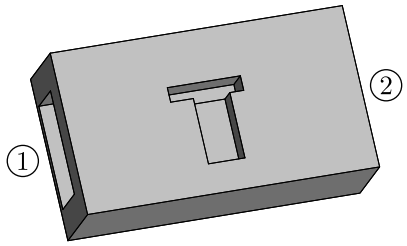

Fig. 1. T-shaped slot fed by a rectangular waveguide.

In this regard, a straightforward approach to attain high-efficiency broadside CP antennas entails adding a polarization conversion mechanism over an all-metal shunt slot array, taking advantage of its good performance and well-known synthesis rules [15]. Different printed geometries have been proposed to play that role, like microstrip patches [16], [17], loops [18] or dipoles [19]–[21]. These printed polarization converters, however, involve some drawbacks in terms of additional dielectric loss, eventual surface-wave propagation or permittivity uncertainty, which often lead to an impairment in antenna efficiency, bandwidth and polarization purity [20].

Some other recent works [22]–[24] propose all-metal polarization converters instead, with an evident benefit in terms of antenna efficiency and reliability. In these cases, each slot feeds an open waveguide, properly shaped to support two orthogonal modes with different enough propagation constants, resulting in very low loss CP radiators. In an array environment, however, this solution leads to bulky structures due to the space constraint when tailoring the waveguides' shape. To give some numbers, the thickness of metallic polarizers in [23], [24] is around $1.5\lambda_0$, unpractical for lower frequency bands.

Following this last strategy, this paper studies a novel all-metal CP radiating element, which reshapes the usual rectangular slot to radiate a CP field. This new solution is only few tenths of wavelength thick, dramatically reducing the required thickness of previous works. When used in an array, these radiating elements can be easily fabricated in a single aluminum piece by conventional CNC machine tools, avoiding eventual field leakage and granting a very high

This work was supported by the Spanish Ministry of Science and Innovation under project PID2019-107688RB-C22.

J. I. Herranz-Herruzo, M. Ferrando-Rocher, A. Valero-Nogueira, and B. Bernardo-Clemente are with the Instituto de Telecomunicaciones y Aplicaciones Multimedia (iTEAM) of the Universitat Politècnica de València, 46022 Valencia, Spain (e-mail: jiherhe@upvnet.upv.es).

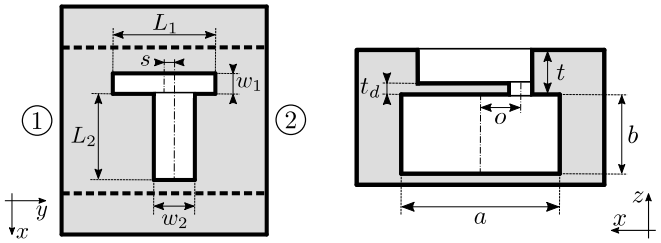

(a) (b)

Fig. 2. Geometry of the T-shaped slot in a rectangular waveguide with all involved dimensions: (a) Top view; (b) Cross-section side view.

antenna efficiency.

The proposed radiator, briefly described as an asymmetric T-shaped slot, is shown in Fig. 1. The thinner arm of the T-shape corresponds to the active slot excited by the rectangular waveguide (RW) field. This slot excites a shifted perpendicular arm, which is actually backshorted and hence not directly fed by the waveguide. It is worth noting here the major difference between this approach and the recent contribution [25], where a symmetric T-slot is proposed. There, both arms of the CP radiator are simultaneously excited by the forward RW mode. Its working principle, in this regard, resembles that of the classic crossed-slot [4], being not valid when fed by a standing-wave mode.

The radiating element studied here was first used in [26] in the context of the so-called gap waveguides, where a very concise description can be found. In this paper, a more general framework is given, presenting the concept as a straightforward way to transform any LP slot array into a CP one. The working principle of the radiator is deeply analyzed in Section II, inspiring an adhoc design process proposed in Section III. A parametric study is carried out in Section IV in order to explore the limits of the polarization bandwidth. Section V examines the new element resonance and addresses the design of resonant shunt arrays, leaving the extension to other array types for future work. Finally, two linear arrays are constructed and measured to assess the manufacturing reliability via conventional milling techniques, as reported in Section VI. Section VII draws the main conclusions.

II. T-Shaped slot

The geometry of the T-shaped slot is drawn in Fig. 2, showing the most relevant dimensions. From the top view in Fig. 2(a), the radiator forms an asymmetric T-shape, comprising two arms not centered along the same axis. The first arm, hereinafter identified as the primary or active slot, is fed by the RW field according to a conventional shunt slot. Although it might be arbitrarily oriented, this longitudinal disposition allows for a shunt array design. As indicated in Fig. 2(a), the dimensions of the primary slot are $L_1 \times w_1$, and o denotes its offset to the waveguide axis.

The second arm of the T-shape acts as a parasitic element, coupled from the primary slot. As can be seen in the side view of Fig. 2(b), this secondary slot is backed by a shortcircuit of thickness t_d. Hence, it can be considered as a blind slot in contrast to the primary arm, to which it is connected

TABLE I
Dimensions of an LHCP T-shaped slot

w_1	L_1	o	t	t_d	w_2	L_2	s
1.0	5.0	1.0	3.5	0.5	2.5	4.937	0.382

Dimensions in millimeters (see Fig. 2) of an LHCP T-shaped slot fed by a WR-28 waveguide (a = 7.112 mm and b = 3.556 mm) at 30 GHz.

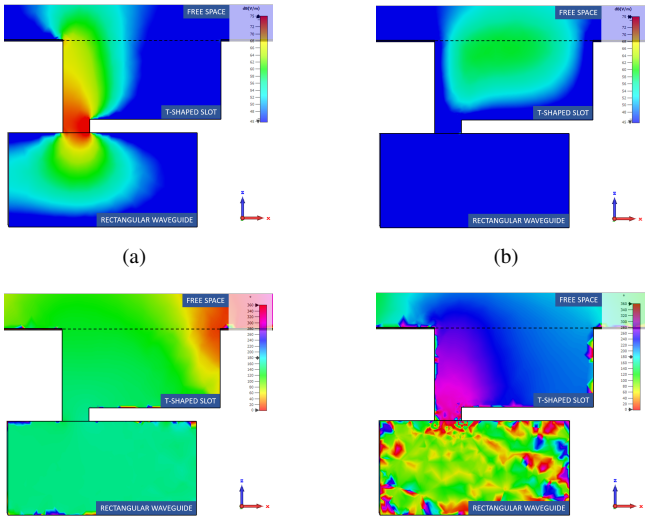

(a) (b) (c) (d)

Fig. 3. Electric field of an LHCP T-shaped slot (Table I) on a xz-plane cross-section at 30 GHz: magnitude (dB) of (a) E_x component and (b) E_y component; phase (degrees) of (c) E_x component and (d) E_y component.

perpendicularly. The dimensions of this slot are $L_2 \times w_2$, and its main axis is shifted a distance s with respect to the primary slot, being t the total thickness of the compound radiator. Note that the secondary arm could extend beyond the waveguide hollow, which may be necessary for negative offsets.

In the following, the working principle and performance of the radiator are shown. For that purpose, Table I defines a baseline T-shaped slot radiating an LHCP field at boresight, and fed by a standard WR-28 waveguide. The working frequency throughout this work has been set to 30 GHz, targeting Ka-band satellite communications. Simulations have been performed by the finite element solver included in CST Studio suite [27].

The polarization conversion mechanism can be readily explained by inspecting how the wave travels from the feeding waveguide to free space. With that aim, the electric field components at 30 GHz are represented in Fig. 3. As can be observed in Fig. 3(a), a strong E_x component is first coupled on the active slot, through which it propagates until it reaches the radiating aperture. Due to the asymmetry of the T-shape, the energy is also coupled from the primary to the secondary arm, this latter acting as a parasitic element. Fig. 3(b) shows that the E_y component is dominant in the secondary arm, roughly behaving as a backshorted half-mode RW. As it will be demonstrated later, the shift parameter s governs how much energy is coupled from the primary to the secondary slot.

The phase distribution of the electric field is determined by slots' lengths, being both around $\lambda_0/2$. On the one hand,

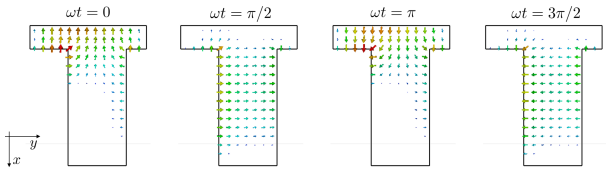

Fig. 4. Instantaneous aperture electric field (xy-plane) at 30 GHz for an LHCP T-shaped slot (Table I).

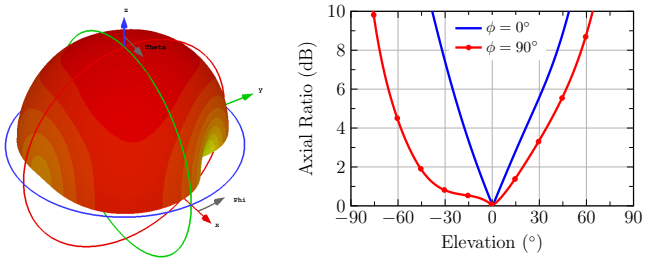

(a) (b)

Fig. 5. (a) Radiation pattern and (b) axial ratio at 30 GHz for the T-shaped slot (Table I).

the RW equivalent to the active slot is around cutoff and therefore the phase of the E_x component barely changes along z direction, as seen in Fig. 3(c). The E_y component, on the other hand, exhibits an appreciable phase delay when it propagates from the parasitic slot backshort to the radiating aperture, as shown in Fig. 3(d). Hence, the initial phase difference around 180º between both components becomes the required 90º value for CP radiation. The described disparity between the two slots, despite its similar length, is due to the fact that the secondary slot actually behaves as a larger RW. This peculiarity allows to achieve an effective CP conversion with a much thinner structure, when compared to previous works [23], [24]. Typically, the additional thickness needed here for polarization conversion is around $0.3\lambda_0$.

The instantaneous electric field on the T-shaped aperture (xy-plane) is shown in Fig. 4. It can be observed how the E-field rotates following the left-hand rule. As seems obvious, this whole study would be valid for an RHCP radiating element too. By mirroring the T-shape along the y-axis ($s < 0$), the same slot will radiate an RHCP field, whereas a completely symmetric T-shape ($s = 0$) will become an LP radiator.

Finally, the radiation pattern of the LHCP T-slot at 30 GHz is shown in Fig. 5(a). A quite omnidirectional radiation is observed, with a maximum directivity of 5.6 dBi, similar to a half-wavelength slot. The AR parameter in both cuts is plotted in Fig. 5(b), exhibiting an expected broadside null. Because of the asymmetry of the T-shaped slot, the AR behaves rather differently along both cuts, being the AR beamwidth much wider along yz-plane. This asymmetry, though, will not have a noticeable effect on the design of directive broadside arrays.

III. Slot Design

An effective CP polarization conversion can be reached just by tuning the length L_2 and shift s of the parasitic slot. Fig. 6 shows a contour plot of the broadside AR versus those

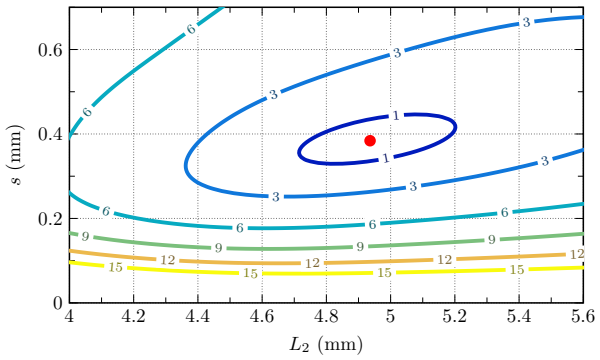

Fig. 6. Axial ratio (dB) at $\theta = \phi = 0º$ for the T-shaped slot (Table I) versus the secondary slot length and shift at 30 GHz.

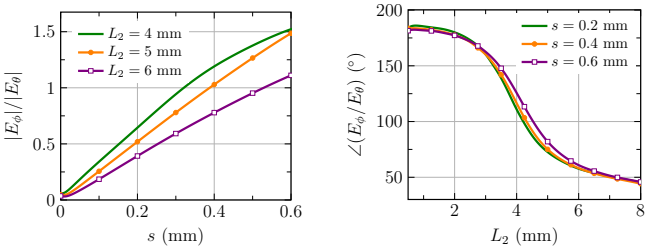

(a) (b)

Fig. 7. Ratio E_ϕ/E_θ of radiated field components at $\theta = \phi = 0º$ for the T-shaped slot (Table I) at 30 GHz: (a) magnitude vs. secondary slot shift and (b) phase vs. secondary slot length.

parameters. A local minimum of 0 dB is found for the nominal values given in Table I, marked as a red dot. As can be seen, the AR function behaves smoothly, and a minimization approach could be applied to find the optimum parameter values. However, the insight given previously allows us to define a more suitable optimization process.

Fig. 7(a) represents the ratio $|E_\phi|/|E_\theta|$ of the radiated components versus the shift s for different lengths L_2. This graph reveals that such ratio increases linearly for larger shifts, entailing a stronger excitation of the secondary slot. In contrast, the phase difference between components, shown in Fig. 7(b), is mostly driven by the secondary slot length L_2 following a similar evolution. For small L_2 values, both slots are below cutoff, so the phase difference remains stable around 180º, given by the initial coupling. From a certain L_2 onward, the secondary slot allows mode propagation and the phase difference starts to decrease continuously.

Figs. 7(a) and 7(b) reveal that magnitude and phase of the components ratio exhibit both a smooth variation around the optimum value, i.e. the unit and 90º, respectively. This fact makes the design process of the secondary slot well suited for a fast optimization routine. Among many options available, the secant method is chosen due to the linearity of the goal functions. Two one-variable search methods are carried out sequentially. The first one seeks to attain a magnitude ratio equal to the unit whereas the second one searches for a phase difference of 90º by tuning s and L_2 values, respectively. The described approach finds the optimum pair (s, L_2) with high precision in a few iterations. Note that the convergence of a

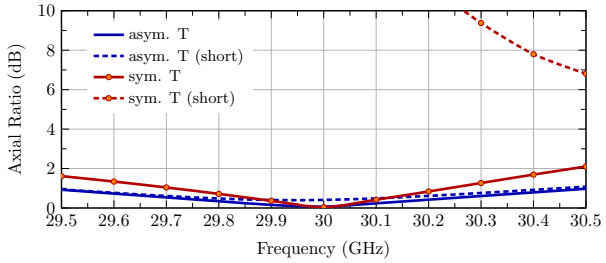

Fig. 8. Axial ratio versus frequency for the asymmetric and symmetric T-shaped slot in an infinite and shorted waveguides.

TABLE II
OPTIMIZED DIMENSIONS (MM) VERSUS PARAMETER VARIATIONS

w_2	1.0	1.5	2.0	2.5	3.0	3.5
L_2	3.870	4.129	4.496	4.937	5.420	5.979
s	0.299	0.311	0.336	0.382	0.475	0.697
t	3.0	3.5	4.0	4.5		
L_2	6.073	4.937	4.422	4.072		
s	0.596	0.382	0.286	0.222		

Optimized dimensions (s, L_2) in millimeters of an LHCP T-shaped slot for the parametric study: variation of parameter w_2 (above) and t (below).

two-variable optimization process over the AR itself in Fig. 6 would be noticeably slower.

It is worth stressing that this design process remains valid when the waveguide mode is modified, since the parasitic slot is coupled to the fundamental mode of the active slot. Such feature is one of the main advantages of the proposed CP radiating element, extending its applicability to different types of slot arrays. For demonstration, Fig. 8 plots the AR frequency sweep comparing two scenarios: when the T-slot is fed by an infinite RW or by a shorted RW (port 2 matched or shorted in Fig. 1). Despite the AR is optimized for the first case, the T-slot preserves the CP radiation capability when excited by a resonant mode. This good property contrasts with the performance of the symmetric T-slot in [25], also shown in Fig. 8. In that case, the optimized AR performance is spoiled when the element is excited by a standing-wave mode.

IV. PARAMETRIC STUDY

A parametric study is carried out now to find design guidelines aiming to maximize the AR bandwidth. In this case, the radiation and impedance bandwidths are not analyzed since they depend on the feeding mechanism of the eventual array. The frequency range from 29.5 GHz to 30.5 GHz is set as reference. Taking the T-slot of Table I as the baseline configuration, each parameter is varied and the pair (s, L_2) is tuned accordingly by following the above design process.

In the first place, the variation of parameter w_2 is studied in Fig. 9(a). It is clearly seen that wider secondary slots provide larger AR bandwidths, but at the expense of longer lengths L_2 (see Table II). A clear tradeoff is therefore revealed between polarization bandwidth and radiator size, which will be a limitation for closely-spaced array elements. Conversely,

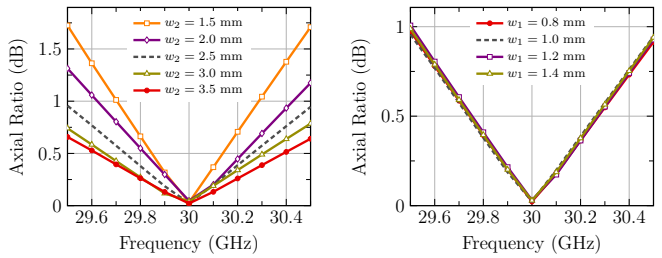

Fig. 9. Axial ratio versus frequency for the optimized T-shaped slot by varying: (a) the secondary and (b) the primary slot width.

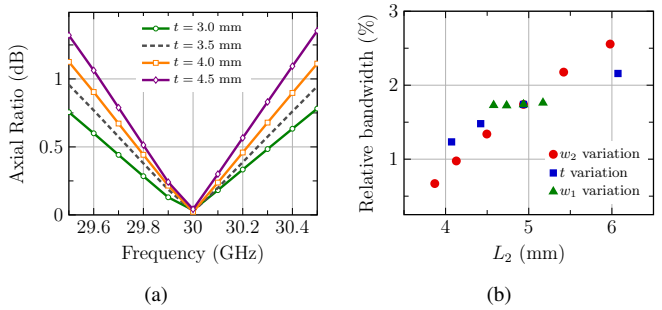

Fig. 10. (a) Axial ratio versus frequency for the optimized T-shaped slot by varying the slot thickness; (b) Relative axial ratio bandwidth below 0.5 dB versus the secondary slot length for different parameter variations.

the AR bandwidth remains virtually unchanged regardless of the active slot width w_1, as shown in Fig. 9(b).

Lastly, the impact of slot thickness t on AR bandwidth is evaluated in Fig. 10(a). It is demonstrated that thicker slots provide wider AR bandwidths but needing again larger L_2 values, as shown in Table II. This trend is consistent with the fact that the equivalent RW moves away from the cutoff. In this regard, Fig. 10(b) marks the relative AR bandwidth below 0.5 dB versus parameter L_2 for all cases addressed. This graph reveals that, in pursuit of a given enhancement of AR bandwidth, it is advisable increasing parameter w_2 to achieve more compact radiating elements.

V. DESIGN OF RESONANT ARRAYS

Once the design and performance of the T-shaped slot have been presented, its capability to set up slot arrays is addressed. This paper focuses on the design of resonant shunt arrays given their simple synthesis by means of a circuit equivalence [15].

A. Single-slot resonance

A single T-shaped slot is studied first to evaluate the effect of the secondary arm on the element resonance. Fig. 11(a) plots the S_{11}-parameter versus frequency, comparing the baseline T-slot with the active slot alone. The latter behaves as a conventional shunt slot resonating around 28.5 GHz. When this slot is loaded with the parasitic arm, the resonance moves up to 31.9 GHz, with a similar conductance, given by the S_{11} real part. It is worth confirming that the T-slot meets the condition $S_{21} = 1 + S_{11}$, so it can also be circuit-modeled as a shunt admittance.

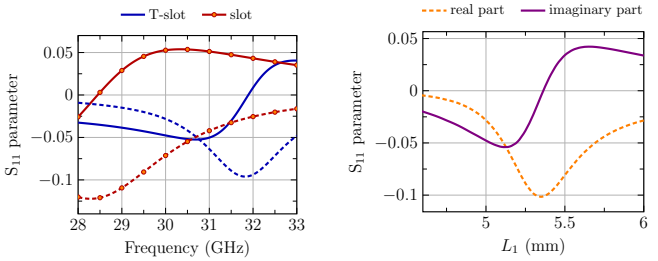

Fig. 11. (a) S_{11}-parameter versus frequency for the T-shaped slot and the single active slot: real (solid) and imaginary part (dashed); (b) S_{11}-parameter at 30 GHz for the T-shaped slot varying the active slot length.

TABLE III
OPTIMIZATION PROCESS OF A RESONANT T-SLOT

	L_2 (mm)	s (mm)	L_1 (mm)	AR (dB)	Im(S_{11})
0. Initial	5.000	0.300	5.000	1.971	-0.207
1. AR opt.	**4.830**	**0.421**	5.200	0.031	-0.041
2. S_{11} opt.	4.830	0.433	**5.348**	0.642	-0.004
3. AR opt.	**4.767**	**0.455**	5.348	0.018	-0.003

Example of iterative optimization process for the T-shaped slot (Table I) showing the parameters involved and the goal functions in each stage.

Therefore, the conventional design of resonant shunt arrays can be applied. As an example, Fig. 11(b) plots the reflection coefficient versus L_1 value at 30 GHz. It is found that the resonant length L_1 is around 5.36 mm, for which the normalized shunt admittance is $\bar{Y}^{\text{sh}} \approx 0.22$. Thanks to the well-behaved linear variation of the S_{11} imaginary part around the resonance, a secant method is also applied here to search the resonant L_1 value.

An iterative design process has been conceived in order to attain a CP resonant T-slot. Starting from an initial parameter set, the AR is optimized by following the process described in Section III, returning a (s, L_2) pair. Next, parameter L_1 is tuned looking for its resonant value. These two processes are repeated until convergence on AR and S_{11} imaginary part. Table III details the involved parameters in an example optimization process, and the evolution of both goal functions. In most cases, as in this one, convergence is reached after three stages. This process is repeated for an offset range, giving as a result the Table IV. This look-up table returns, for each conductance needed in the array synthesis, the length L_1 and offset o of the active slot and the length L_2 and shift s of the parasitic slot. These parameters follow a fairly linear dependence on the offset, appropriate for the required interpolation.

B. Periodic model

The described design process remains valid when periodic boundary conditions are considered to account for mutual coupling. In this case, an infinite shunt linear array is emulated by defining four different 2-slot periodic cells. The first two options in Figs. 12(a) and 12(b) consider one active port, placing a load or a short on the opposite side of the

TABLE IV
DESIGN TABLE OF A RESONANT T-SLOT

o (mm)	**0.50**	**0.75**	**1.00**	**1.25**	**1.50**
L_1 (mm)	5.220	5.281	5.348	5.437	5.493
L_2 (mm)	4.792	4.774	4.767	4.733	4.723
s (mm)	0.423	0.438	0.455	0.480	0.494
$\bar{Y}^{\text{sh}}$	0.053	0.115	0.185	0.243	0.303

Design table of a resonant T-shaped slot (Table I) as a function of the offset.

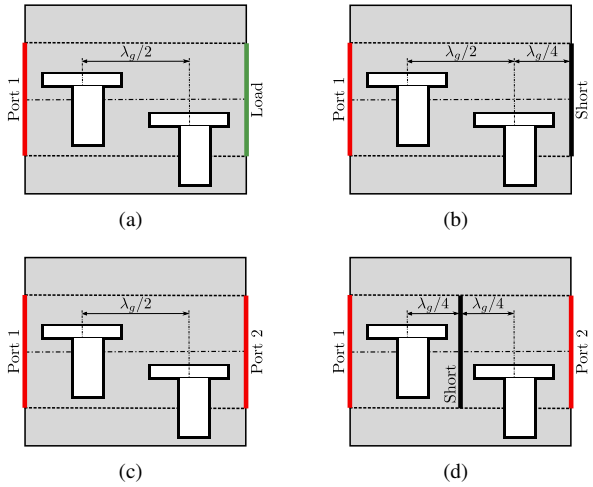

Fig. 12. Four different periodic cells: (a) 1 port and a matched load; (b) 1 port and a short; (c) 2 ports; (d) 2 ports and a middle short.

waveguide, respectively. The third model in Fig. 12(d) simulates a symmetric problem by defining two active ports and placing a short between the two slots. This choice was used in [28]. Alternatively, the fourth cell in Fig. 12(c) generates a standing-wave mode without a short by exciting both ports with opposite phases. In all four cases, slot admittances are extracted from simulated S-parameters via a simple circuit analysis, omitted here for brevity.

To assess the accuracy of the conductance table provided by the four periodic models, a uniform 1×10 linear array is designed. The frequency sweep of the reflection coefficient, plotted in Fig. 13(a), evidences that the proposed 2-port model without short provides the best performance in terms of resonance frequency and S_{11} level. The first 1-port model with a matched load also yields a quite satisfactory result in contrast to the two models with shortcircuits. The inaccuracy of these latter comes from an imprecise characterization of internal coupling. Note that, applying image theory, slots next to a short will have a virtual neighbor on the same side of the waveguide axis, unlike the actual array. Finally, regarding the AR sweep shown in Fig. 13(b), all four models exhibit good results, although the 2-port cell without short again provides the best design accuracy. The latter will be used hereinafter.

The pattern synthesis is now evaluated by designing two 10-element linear arrays: one uniform and the other implementing a 20 dB Taylor distribution. In both cases, radiation patterns at the design frequency, plotted in Fig. 14, behave as expected with well-shaped lobes and a crosspolar broadside

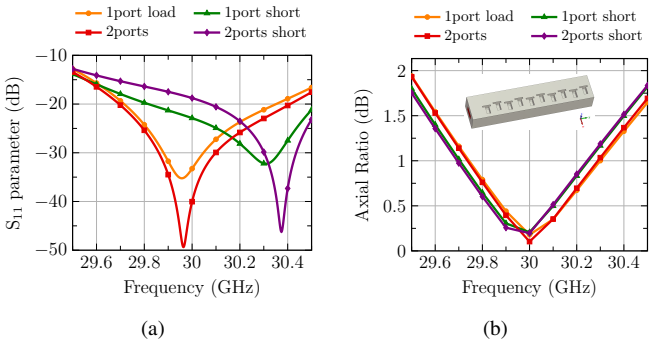

Fig. 13. Design results provided by the four periodic models for a ten-element uniform linear array of T-shaped slots: (a) reflection coefficient and (b) axial ratio versus frequency.

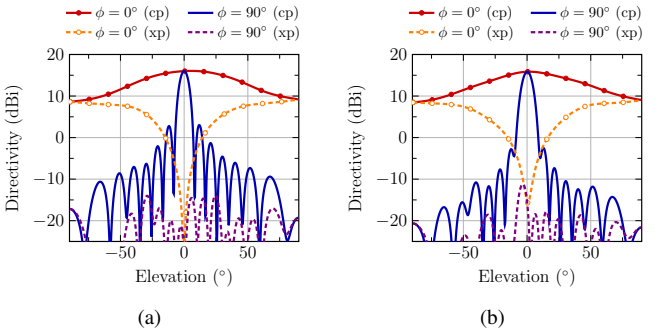

Fig. 14. Copolar (cp) and crosspolar (xp) radiation pattern at 30 GHz of a 10-element linear array of T-shaped slots: (a) uniform; (b) 20 dB Taylor distribution.

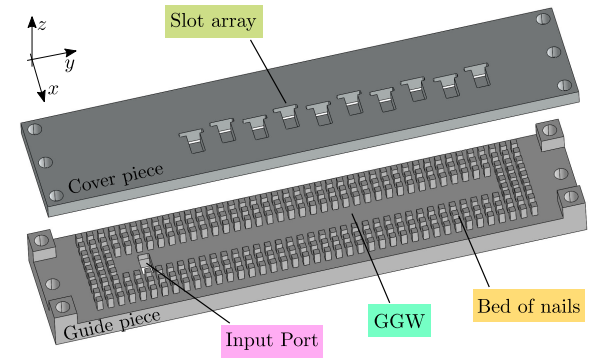

Fig. 15. Exploded view of the fabricated linear array.

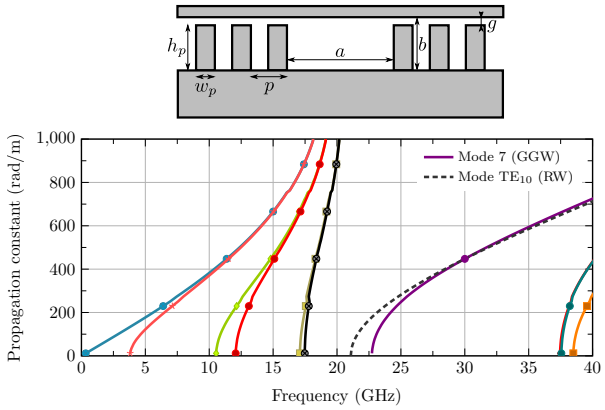

Fig. 16. Dispersion diagram of the groove-gap waveguide. The parameters used are: a = 7.112 mm, b = 3.556 mm, h_p = 3 mm, w_p = 1.25 mm, p = 2.4 mm, g = 0.556 mm.

null. Sidelobe level (SLL) is -13.0 dB and -18.5 dB for uniform and Taylor arrays, respectively. Despite the latter remains 1.5 dB above specification, a satisfactory design is achieved, considering the relatively low number of elements. A better match to the theoretical SLL would require an optimization process, not addressed here.

VI. Experimental Validation

The suitability of the proposed radiating element to be fabricated via conventional milling techniques with standard tolerances is now validated. With that aim, a 1×10 linear array has been constructed and tested, depicted in Fig. 15 in an exploded view. In order to prevent any eventual field leakage, the feeding RW is replaced by a groove-gap waveguide (GGW) [29]. In this way, the antenna can be easily manufactured in two separate pieces and assembled with just four screws. The bottom piece includes the bed of nails surrounding the waveguide and the input port, while the T-shaped slots are milled on the cover piece.

GGW waveguides have demonstrated to be a convenient and seamless replacement for RWs in series-fed arrays [20], [30]. The chosen GGW replicates the main dimensions (a, b) of the standard WR-28, leaving a gap of g = 0.556 mm with the top metal lid. Fig. 16 shows the GGW dispersion diagram together with its main dimensions, proving that only one mode can propagate through the GGW within a large bandwidth around 30 GHz. This mode can be assumed to be equivalent to the TE_{10} mode in the WR-28 waveguide at 30 GHz, with a roughly similar field distribution and identical propagation constant, as demonstrated in Fig. 16.

The waveguide edge feeding used so far in simulations has been replaced by a WR-28 back port, more convenient for radiation measurements. A stepped transition between the input port and the GGW has been optimized resulting in the frequency response plotted in Fig. 17. The simulated reflection coefficient remains below -25 dB in the band of interest.

Once the input port and the feeding waveguide are defined, two different 10-element linear arrays are tested. Two covers were fabricated, one for each array, but sharing the same feeding waveguide. The first one corresponds to a uniform array while the second one synthesizes a 20 dB Taylor distribution. According to the previous findings, the parasitic slot width has been increased to enhance the AR bandwidth. The rest of parameters remain unchanged, namely w_1 = 1 mm, t = 3.5 mm, t_d = 0.5 mm and w_2 = 3 mm.

Some pictures of the manufactured prototype are shown in Fig. 18. The three pieces have been fabricated by a CNC milling machine. For the uniform array, the design process delivers identical T-shaped slots with dimensions o = 0.528 mm, L_1 = 5.335 mm, L_2 = 5.107 mm and s = 0.297 mm. In the case of the Taylor array, the dimensions of each element are indicated in Table V.

The measured and simulated reflection coefficient of both

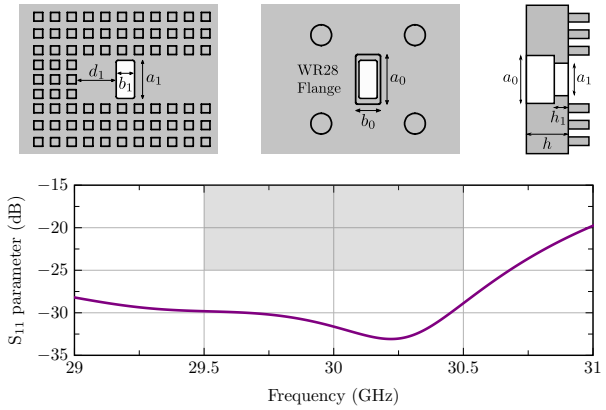

Fig. 17. Reflection coefficient versus frequency of the transition from the WR-28 input port to the GGW. The parameters used are: a_0 = 7.112 mm, b_0 = 3.556 mm, a_1 = 5.421 mm, b_1 = 2.600 mm, d_1 = 5.755 mm, h_1 = 1.666 mm, h = 5.5 mm.

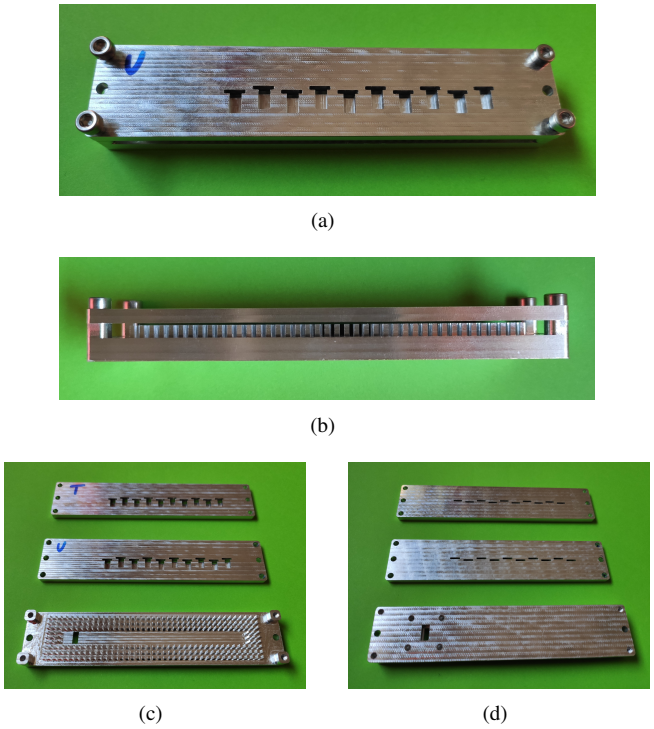

(a)

(b)

(c) (d)

Fig. 18. Pictures of the manufactured prototype: (a) top and (b) side view of the assembly; (c) top and (d) rear view of the three fabricated pieces. Uniform and Taylor array covers are marked U and T, respectively.

arrays is plotted in Fig. 19. A very good agreement is found despite the measured resonance is not as deep as predicted by simulation, reaching a minimum S_{11} level around -20 dB. Both measured responses are practically identical, revealing a very good fabrication repeatability. The measured -10 dB bandwidth is 1.25 GHz, very similar to the simulated one.

The measured boresight AR versus frequency is plotted in Fig. 20. Compared to simulation, a very good agreement is found, particularly for the Taylor array, with a slight frequency shift for the uniform version. The overall performance, however, can be rated as very satisfactory, with a measured AR bandwidth even better than that given by simulation.

TABLE V
DIMENSIONS (MM) OF TAYLOR LINEAR ARRAY

# Slot	1	2	3	4	5
o	-0.344	0.427	-0.532	0.621	-0.671
L_1	5.240	5.302	5.337	5.357	5.368
L_2	5.128	5.113	5.092	5.082	5.078
s	0.273	0.280	0.285	0.291	0.295

Dimensions in millimeters of the T-shaped slots of the fabricated Taylor array. The parameters from the 6th to 10th slot are mirrored.

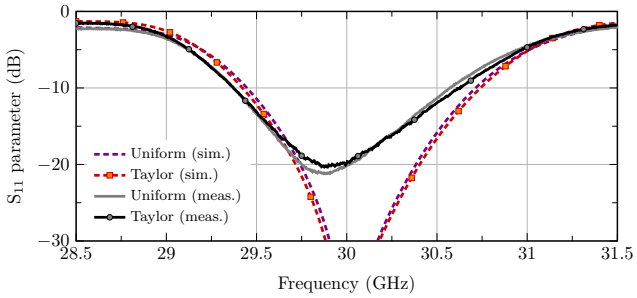

Fig. 19. Measured and simulated reflection coefficient.

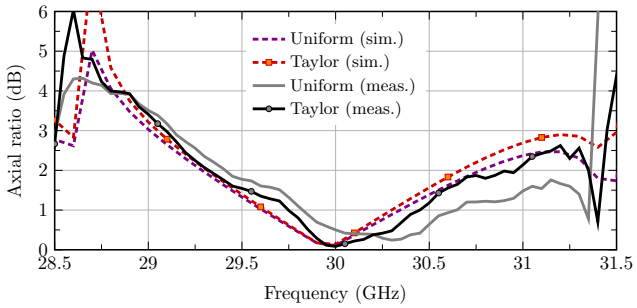

Fig. 20. Measured and simulated broadside axial ratio versus frequency.

The measured AR keeps below 1 dB within a bandwidth of 0.70 GHz and 0.83 GHz for the uniform and Taylor arrays, respectively. If the accepted threshold moves up to 2 dB, those bandwidths are respectively 1.65 GHz and more than 1.9 GHz. The minimum measured AR value also evidences the good fabrication accuracy, being 0.24 dB for the uniform array and 0.08 dB for the Taylor sample.

A conventional far field measurement is conducted to sample the radiation patterns of both antennas, which are plotted in Figs. 21 and 22 at 30 GHz. A very good match is evidenced between simulation and measurement both in copolar and crosspolar components. Along the directive cut, the uniform array presents a well-shaped pattern in Fig. 21(b), with a measured SLL of -13.7 dB and a maximum directivity around 17 dBi, very close to the theoretical values. As for the Taylor array, Fig. 22(b) also includes the computed array factor corrected by the cosine function. Compared to this theoretical result, a null-filling effect is measured in the first sidelobes, as predicted by simulation. In this case, the measured SLL is -18.5 dB, 1.5 dB above specification, and the maximum directivity is 16.3 dBi. Concerning the not directive cut, the measured pattern displays the typical ripple near

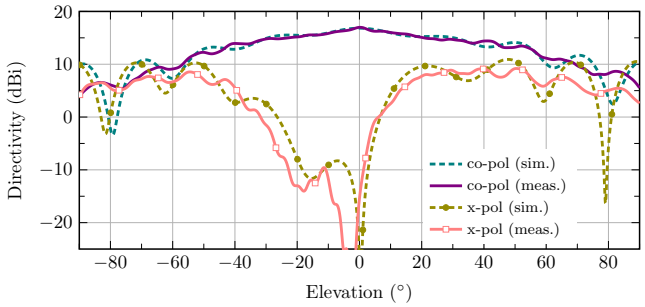

(a)

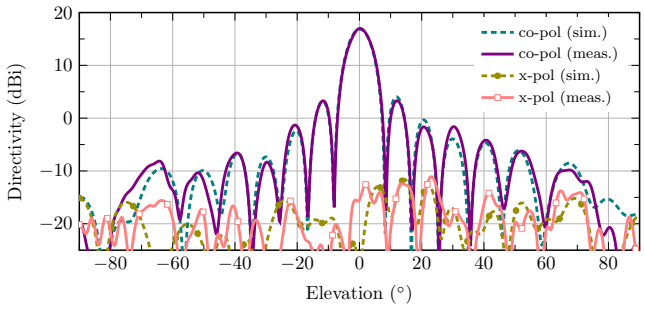

(b)

Fig. 21. Measured and simulated radiation pattern at 30 GHz for the uniform array: (a) $\phi = 0°$; (b) $\phi = 90°$.

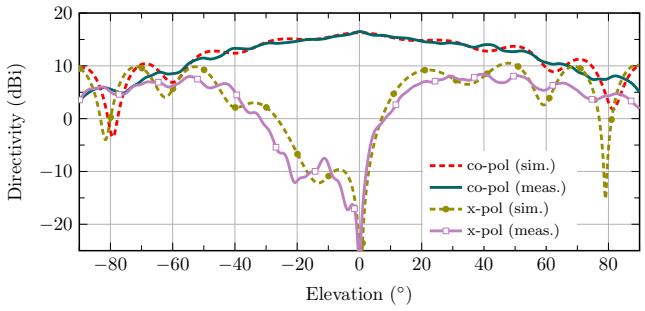

(a)

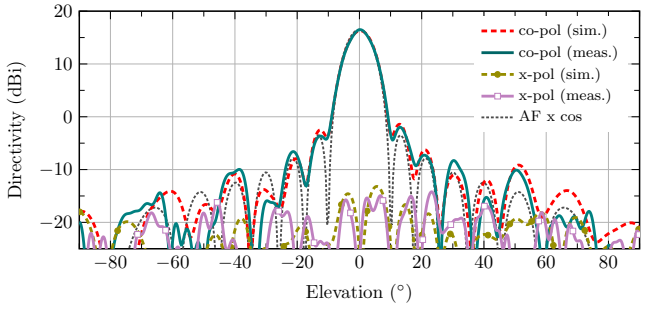

(b)

Fig. 22. Measured and simulated radiation pattern at 30 GHz for the Taylor array: (a) $\phi = 0°$; (b) $\phi = 90°$.

endfire, attributed to the edge diffraction, while the crosspolar component exhibits the expected broadside null.

For the sake of completeness, the measured copolar radiation pattern is plotted at equispaced frequencies within the operation band in Fig. 23. Measured patterns behave as

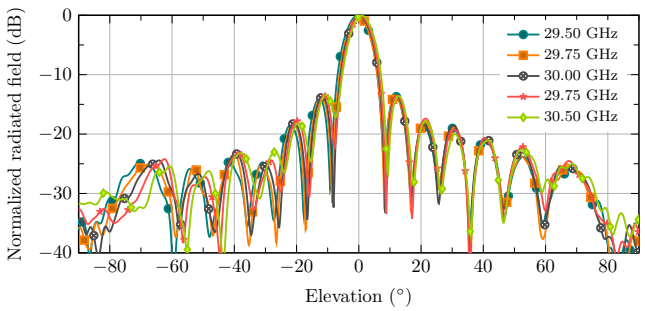

(a)

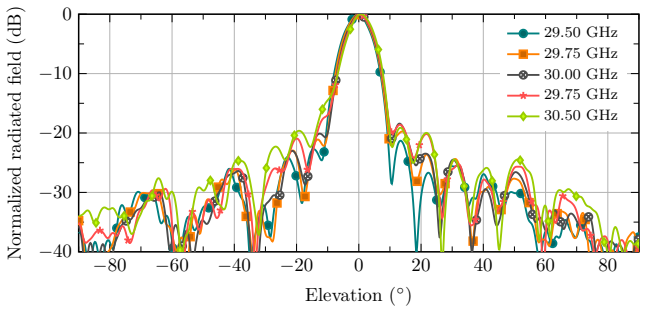

(b)

Fig. 23. Measured copolar radiation patterns at equispaced frequencies around 30 GHz in $\phi = 90°$ plane: (a) uniform array; (b) Taylor array.

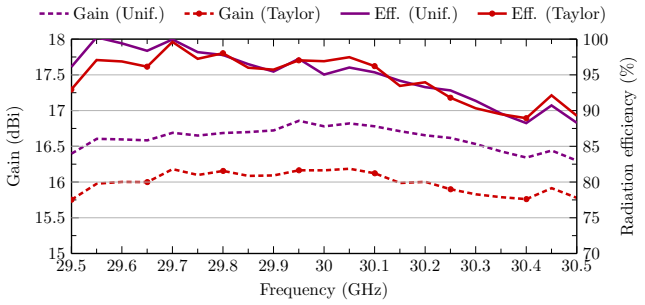

Fig. 24. Measured gain and radiation efficiency versus frequency.

expected, showing a very slight beam squint but preserving the sidelobe level. As it is already known, a wider radiation and impedance bandwidth would be attained by reducing the number of elements or adopting a center feeding approach.

Finally, the gain has been experimentally evaluated by comparison with a standard LP horn in both polarizations. Fig. 24 represents the measured total gain and radiation efficiency of both antennas within the matched frequency band. Because of their all-metal nature, both arrays present a remarkably high radiation efficiency, around 98% in the lower part of the band.

The main characteristics of the proposed antenna are compared in Table VI to the most relevant mm-wave broadside CP arrays formed by all-metal radiating elements. Similarly to this work, the first three references [22]–[24] include metallic polarizers over slots. Despite reaching comparable or even much lower AR bandwidths, those antennas needed a much thicker and heavier polarizer than the solution here proposed. The radiating element proposed in [25], apparently similar to this work, relies on a completely different working principle

TABLE VI
COMPARISON OF MM-WAVE CP WAVEGUIDE SLOT ARRAYS

Ref.	Feeding network	Radiating element	Number of layers	Number of elements	Frequency	Radiator thickness	Impedance bandwidth	AR 3dB bandwidth	Min. AR	Peak efficiency
[22]	Series RW	Open GW	1	1×12	30 GHz	n.a.	1%	4%	0.5 dB	n.a.
[23]	Corporate GGW	Open GW	1	16×16	60 GHz	$1.4\lambda_0$	11%	8%	1.8 dB	83%
[24]	Corporate SIW	Open GW	3	4×4	35 GHz	$1.75\lambda_0$	1%	1%	0.5 dB	n.a.
[25]	Corporate RW	T-shaped slot	3	6×8	30 GHz	n.a.	3%	1%	1 dB	n.a.
[1]	Corporate-SR RGW	Chamfered slot	2	8×8	30 GHz	$0.6\lambda_0$	22%	22%	0 dB	85%
[8]	Corporate-SR SIW	ME dipole	3	4×4	27 GHz	$0.15\lambda_0$	28%	28%	0.5 dB	78%
This work	Series GGW	T-shaped slot	1	1×10	30 GHz	$0.3\lambda_0$	4%	8%	0.1 dB	98%

though. This fact is evidenced by the narrow AR bandwidth of 1% compared to that achieved here, around 8%.

Lastly, two completely different approaches [1], [8] are also included in the comparison, both employing the sequential rotation (SR) technique to reach outstanding AR bandwidths. These antennas make use of an intricate multilayer feeding network, which inevitably hampers its design and fabrication process, in addition to increasing waveguide losses. As a result of its simple feeding mechanism, the antenna presented here clearly exhibits lower AR and impedance bandwidths, but higher antenna efficiency and low-sidelobe design capability. The extension of this T-shaped radiating element to be used in wideband corporate-fed arrays is left for future work.

VII. CONCLUSIONS

This paper proposes a novel T-shaped radiating element suitable for all-metal circularly-polarized slot arrays. The proper inclusion of a perpendicular arm coupled to a rectangular slot enables the linear-to-circular polarization conversion, thus avoiding the use of printed structures. Compared to previous similar concepts, this element is able to achieve an effective CP conversion with a much lower profile structure. The suitability of the concept has been experimentally tested, finding a very good reliability and repeatability when fabricated via conventional milling techniques.

Experimental results confirm the good CP polarization purity and the high efficiency reached by this new radiating element, being a promising solution to replace slots in large all-metal arrays. Its versatility enables the design of low-sidelobe or shaped-beam CP arrays with little increase in antenna thickness compared to LP arrays. The concept can also be extended to wideband corporate-fed arrays in order to increase the radiation and impedance bandwidths. The attainable polarization bandwidth may be enough for a large variety of applications, including radar or satellite communications, and its all-metal nature grants a high-efficiency performance at high-frequency bands.

REFERENCES

[1] M. Akbari, A. Farahbakhsh, and A. Sebak, "Ridge gap waveguide multilevel sequential feeding network for high-gain circularly polarized array antenna," *IEEE Trans. Antennas Propag.*, vol. 67, no. 1, pp. 251–259, 2019.

[2] J. Wu, Y. J. Cheng, H. B. Wang, Y. C. Zhong, D. Ma, and Y. Fan, "A wideband dual circularly polarized full-corporate waveguide array antenna fed by triple-resonant cavities," *IEEE Trans. Antennas Propag.*, vol. 65, no. 4, pp. 2135–2139, 2017.

[3] M. Ferrando-Rocher, J. I. Herranz-Herruzo, A. Valero-Nogueira, and A. Vila-Jiménez, "Single-layer circularly-polarized ka -band antenna using gap waveguide technology," *IEEE Trans. Antennas Propag.*, vol. 66, no. 8, pp. 3837–3845, 2018.

[4] J. Hirokawa, M. Ando, N. Goto, N. Takahashi, T. Ojima, and M. Uematsu, "A single-layer slotted leaky waveguide array antenna for mobile reception of direct broadcast from satellite," *IEEE Trans. Veh. Technol.*, vol. 44, no. 4, pp. 749–755, 1995.

[5] X. Huo, J. Wang, D. Li, Z. Zhang, M. Chen, and Z. Li, "Leaky rectangular waveguide with circular polarization property," *IEEE Trans. Antennas Propag.*, vol. 63, no. 11, pp. 5098–5101, 2015.

[6] L. Zhang, K. Wu, S. Wong, Y. He, P. Chu, W. Li, K. X. Wang, and S. Gao, "Wideband high-efficiency circularly polarized siw-fed s-dipole array for millimeter-wave applications," *IEEE Trans. Antennas Propag.*, vol. 68, no. 3, pp. 2422–2427, 2020.

[7] Y. Zhang, W. Hong, and R. Mittra, "45 ghz wideband circularly polarized planar antenna array using inclined slots in modified short-circuited siw," *IEEE Trans. Antennas Propag.*, vol. 67, no. 3, pp. 1669–1680, 2019.

[8] B. Feng, J. Lai, K. L. Chung, T. Y. Chen, Y. Liu, and C. Y. D. Sim, "A compact wideband circularly polarized magneto-electric dipole antenna array for 5g millimeter-wave application," *IEEE Trans. Antennas Propag.*, vol. 68, no. 9, pp. 6838–6843, 2020.

[9] J. Xu, W. Hong, Z. H. Jiang, and H. Zhang, "Low-cost millimeter-wave circularly polarized planar integrated magneto-electric dipole and its arrays with low-profile feeding structures," *IEEE Antennas Wireless Propag. Lett.*, vol. 19, no. 8, pp. 1400–1404, 2020.

[10] M. Ando, K. Sakurai, N. Goto, K. Arimura, and Y. Ito, "A radial line slot antenna for 12 ghz satellite tv reception," *IEEE Trans. Antennas Propag.*, vol. 33, no. 12, pp. 1347–1353, 1985.

[11] G. Montisci, "Design of circularly polarized waveguide slot linear arrays," *IEEE Trans. Antennas Propag.*, vol. 54, no. 10, pp. 3025–3029, 2006.

[12] M. Al Sharkawy and A. A. Kishk, "Wideband beam-scanning circularly polarized inclined slots using ridge gap waveguide," *IEEE Antennas Wireless Propag. Lett.*, vol. 13, pp. 1187–1190, 2014.

[13] M. M. Sabahi, A. A. Heidari, and M. Movahhedi, "A compact crlh circularly polarized leaky-wave antenna based on substrate-integrated waveguide," *IEEE Trans. Antennas Propag.*, vol. 66, no. 9, pp. 4407–4414, 2018.

[14] S. Chen, D. K. Karmokar, Z. Li, P. Qin, R. W. Ziolkowski, and Y. J. Guo, "Circular-polarized substrate-integrated-waveguide leaky-wave antenna with wide-angle and consistent-gain continuous beam scanning," *IEEE Trans. Antennas Propag.*, vol. 67, no. 7, pp. 4418–4428, 2019.

[15] R. S. Elliott, "The design of waveguide-fed slot arrays," in *Antenna handbook*. Springer, 1988, pp. 805–842.

[16] T. Li, B. Wang, and W. Dou, "Substrate integrated waveguide slot array antenna covered by circularly polarised array patches," *Electronics Letters*, vol. 51, no. 21, pp. 1634–1635, 2015.

[17] J. Xu, M. Wang, H. Huang, and W. Wu, "Circularly polarized patch array fed by slotted waveguide," *IEEE Antennas Wireless Propag. Lett.*, vol. 14, pp. 8–11, 2015.

[18] L. Lu, Y. Jiao, Z. Weng, H. Zhang, and C. Cui, "Design of low-sidelobe

circularly polarized loop linear array fed by the slotted siw," *IEEE Antennas Wireless Propag. Lett.*, vol. 16, pp. 537–540, 2017.

[19] M. Ferrando-Rocher, J. I. Herranz-Herruzo, A. Valero-Nogueira, and V. M. Rodrigo, "Circularly polarized slotted waveguide array with improved axial ratio performance," *IEEE Trans. Antennas Propag.*, vol. 64, no. 9, pp. 4144–4148, 2016.

[20] J. I. Herranz-Herruzo, A. Valero-Nogueira, M. Ferrando-Rocher, B. Bernardo, A. Vila, and R. Lenormand, "Low-cost ka-band switchable rhcp/lhcp antenna array for mobile satcom terminal," *IEEE Trans. Antennas Propag.*, vol. 66, no. 5, pp. 2661–2666, 2018.

[21] J. Cao, H. Wang, S. Mou, P. Soothar, and J. Zhou, "An air cavity-fed circularly polarized magneto-electric dipole antenna array with gap waveguide technology for mm-wave applications," *IEEE Trans. Antennas Propag.*, vol. 67, no. 9, pp. 6211–6216, 2019.

[22] D. Dogan and C. B. Top, "Circularly polarized ka-band waveguide slot array with low sidelobes," in *2012 6th European Conference on Antennas and Propagation (EUCAP)*, 2012, pp. 1105–1109.

[23] M. Ferrando-Rocher, A. Valero-Nogueira, J. I. Herranz-Herruzo, and J. Teniente, "60 ghz single-layer slot-array antenna fed by groove gap waveguide," *IEEE Antennas Wireless Propag. Lett.*, vol. 18, no. 5, pp. 846–850, 2019.

[24] W. Li, X. H. Tang, and Y. Yang, "A ka-band circularly polarized substrate integrated cavity-backed antenna array," *IEEE Antennas Wireless Propag. Lett.*, vol. 18, no. 9, pp. 1882–1886, 2019.

[25] K. C. Dimitrov, Y. Lee, B. Min, J. Park, J. Jeong, and H. Kim, "Circularly polarized t-shaped slot waveguide array antenna for satellite communications," *IEEE Antennas Wireless Propag. Lett.*, vol. 19, no. 2, pp. 317–321, 2020.

[26] M. Ferrando-Rocher, J. I. Herranz-Herruzo, D. Sánchez-Escuderos, and A. Valero-Nogueira, "A novel circularly-polarized t-shaped slot array antenna in ka-band," in *2020 14th European Conference on Antennas and Propagation (EuCAP)*, 2020, pp. 1–3.

[27] D. Systemes, "Cst microwave studio," *computer program] Available at: http://www. cst. com [Accessed: 11 January 2019]*, 2017.

[28] P. Chen, W. Hong, Z. Kuai, and J. Xu, "A substrate integrated waveguide circular polarized slot radiator and its linear array," *IEEE Antennas Wireless Propag. Lett.*, vol. 8, pp. 120–123, 2009.

[29] P. Kildal, E. Alfonso, A. Valero-Nogueira, and E. Rajo-Iglesias, "Local metamaterial-based waveguides in gaps between parallel metal plates," *IEEE Antennas Wireless Propag. Lett.*, vol. 8, pp. 84–87, 2009.

[30] J. I. Herranz Herruzo, A. Valero-Nogueira, S. Martínez Giner, and A. Vila Jiménez, "Untilted narrow-wall slots excited by parasitic dipoles in groove gap waveguide technology," *IEEE Trans. Antennas Propag.*, vol. 63, no. 11, pp. 4759–4765, 2015.